ELSEVIER

Journal of Volcanology and Geothermal Research 95 (2000) 157–173

Journal of volcanology and geothermal research

www.elsevier.com/locate/jvolgeores

Poisson's ratio and porosity at Coso geothermal area, California

Jonathan M. Lees *, Huatao Wu

Department of Geology and Geophysics, Yale University, New Haven, CT 06510, USA

Received 19 April 1999; received in revised form 2 August 1999; accepted 2 August 1999

Abstract

High-resolution, three-dimensional, compressional and shear wave velocity models, derived from microearthquake traveltimes, are used to map the distribution of Poisson's ratio and porosity at Coso Geothermal Area, Inyo County, California. Spatial resolution of the three-dimensional Poisson's ratio and porosity distributions is estimated to be 0.5 km horizontally and 0.8 km vertically. Model uncertainties, $\pm 1\%$ in the interior and $\pm 2.3\%$ around the edge of the model, are estimated by a jackknife method. We use perturbations of $r = V_p / V_s$ ratio and $\Psi = V_p \cdot V_s$ product to derive distributions of Poisson's ratio, σ, and porosity, which are then used to constrain and delineate possible zones of intense heat, fracture accumulation and fluid saturation. Poisson's ratio at Coso ranges from 0.15 to 0.35 with an average of 0.224, lower than the crustal average of 0.25. High Poisson's ratios are more extensive in shallower depths (< 1.5 km) while lower Poisson's ratios are found in the deeper section (1.5–3.0 km) of the target area. Two major features with low Poisson's ratio are identified at geothermal production depth (1–3 km) around stations S2–S6 and S1–S3–S4. The two low-σ features are separated by a northwest–southeast-trending high-σ belt with variable width of 1–3 km. A high-Ψ body is found around S2 and S6, and extends down in depth. A circular, low-Ψ belt corresponding to the high-σ belt, is located around S2–S6 and is linked to a previously reported structure in V_s tomography. This low-Ψ (highly porous) belt is probably a horizontal conduit/reservoir of geothermal fluid. A vertical, low-σ and high-Ψ channel beneath triangle S1–S3–S4 corresponds to a high-attenuation, dome-like feature. We propose an upwell-and-spread magma intrusion model for the last major magmatism in the Coso region. The magmatic upwelling is centered in the S1–S3–S4 area. The model predicts potential geothermal resources to the south and west of triangle S1–S3–S4 based on local faulting patterns.

Keywords: Poisson's ratio; porosity; Coso geothermal area

1. Introduction

Detailed, three-dimensional heat, fracture, and porosity distributions at Coso geothermal field are crucial to the understanding of geothermal fluid transport and further development of geothermal energy. In this study we use the high-resolution *P*- and *S*-wave velocity models presented previously (Wu and Lees, 1999) to model three-dimensional Poisson's ratio and porosity distributions. The derived models are further related to the distribution of temperature, cracks, rhyolitic domes and observed fluid flows in the geothermal field. We propose in this paper a magmatic intrusion model to summarize

* Corresponding author.

E-mail addresses: lees@hess.geology.yale.edu (J.M. Lees), wu@hess.geology.yale.edu (H. Wu).

0377-0273/00/$ - see front matter
PII: S0377-0273(99)00126-2

the recent geophysical research in this area and to facilitate future investigations.

Estimation of elastic rock parameters using seismic methods is inherently a remote method: We make measurements on arriving waves at the surface and infer from them properties deep within the earth. In the tomographic approach, travel times are used to first estimate the *P*- and *S*-wave velocities, and from these we infer variations of rock lithologies or other physical parameters. Unfortunately, this process leads to non-unique solutions, primarily because many rocks with differing physical states have similar seismic velocities. Indeed, seismic velocity alone is not a sensitive indicator of variable rock property. For this reason it is often useful to consider ratios and products of seismic parameters to differentiate three-dimensional variations in the subsurface. A brief review of how rock properties relate to seismic velocity and attenuation can be found in Sanders et al. (1995). The authors point out that increases in V_p/V_s ratio are related to increases of temperature, and fracture and especially partial melt. Decreases can be associated with the presence of gas or supercritical fluids. In general, V_p and V_s velocities decrease with increasing temperature, but they do so slowly, until they approach the melting point where properties change rapidly. In this paper, we continue the analysis started by (Wu and Lees, 1999) and consider variations of V_p/V_s as well as the product V_pV_s. These different combinations provide a different view of the subsurface variations and are sensitive to different physical effects.

Poisson's ratio can be a useful indicator of lithology and pore fluid pressure and, on average, is ~ 0.25 for Earth's crust and upper mantle (Holbrook et al., 1988). Furthermore, there is a strong dependence of Poisson's ratio on the overall volume of cracks and their aspect ratios (Koch, 1992). Poisson's ratio is directly related to V_p/V_s, the ratio of compressional and shear wave velocities. Traditional methods for computing V_p/V_s, and thus Poisson's ratio, σ, are either direct or indirect. Direct inversion methods estimate V_p and V_s separately, although because of the historical poor quality and low precision observed *S*-wave arrivals, these direct methods have not been reliable in practice. Indirect methods, on the other hand, invert for V_p/V_s using known or assumed *P*-wave velocity models and are more common in the literature (Walck, 1988; Hauksson and Haase, 1997). In a previous, regional analysis of the Coso Field, separate inversions were performed for V_p and then for V_p/V_s (Walck, 1988). However, *P*- and *S*-wave paths, assumed to be identical in the indirect approaches, can be significantly different if the velocity is inhomogeneous and/or V_p/V_s is not constant (Nicholson and Simpson, 1985). In regions with large variations of V_p/V_s, systematic errors introduced by the assumptions can be large. Furthermore, errors in the *P* inversion are propagated into the V_p/V_s inversion through a multiplication and are difficult to quantify. Other deficiencies in the indirect formulation, such as instabilities and inconsistencies, have been noted by (Koch, 1992). These disadvantages diminish significantly the effectiveness of the indirect methods. In the present analysis, we adopt an approach which uses direct methods because we have high-quality *P*- and *S*-wave arrivals.

The product of compressional and shear wave velocities, V_pV_s, on the other hand, has been used to delineate porosity in sedimentary rocks (Iverson et al., 1989). It has been observed that lower V_pV_s indicates an increase of porosity whereas V_p/V_s, constant for a specific lithology, does not change with porosity (Pickett, 1963; Tatham, 1982). Given this fact, V_p/V_s, or σ, is commonly used to delineate lithology while the product V_pV_s can be used to identify variations in porosity (Tatham, 1982; Iverson et al., 1989). In geothermal settings, porosity distributions may be more critical for understanding the physics of the field than lithologic variations. In this paper we will address both.

Our research is made possible by the availability of high-resolution *P*- and *S*-wave velocity models presented previously (Wu and Lees, 1999). The special character of this geothermal dataset derives from the fact that the 16 seismic stations used are borehole installations, allowing for low-noise, high-fidelity recording of incoming seismic waves. Three-component stations are typically located 70 m below the surface, where earthquake events down to magnitude -2 are often recorded in the field. In view of the high-quality dataset in this area, especially the high-quality horizontal *S*-wave arrival picks, we adopt a direct approach to compute V_p/V_s avoiding the complications described above inherent in the, more

commonly used, indirect approach. Our results relate the three-dimensional variations in V_p/V_s and V_pV_s to fluctuations in fluid content and porosity.

2. Velocity inversion of microseismic data

The Coso geothermal area, California (Fig. 1), is located between the extensional basin and range provinces and dextral strike–slip San Andreas faulting system (Duffield and Bacon, 1981). See Reasenberg et al. (1980) and Wu and Lees (1999) for a brief description of local geology and a review of previous geophysical research in the area. Recent attenuation and local stress studies reveal structural details related to geothermal activity and associated extraction of fluids from the field (Wu and Lees, 1996; Feng and Lees, 1998). Variations of stress at Coso agree with regional extensional stress for the most part, although the southwestern cluster of seismicity appears to have a more horizontal principal stress

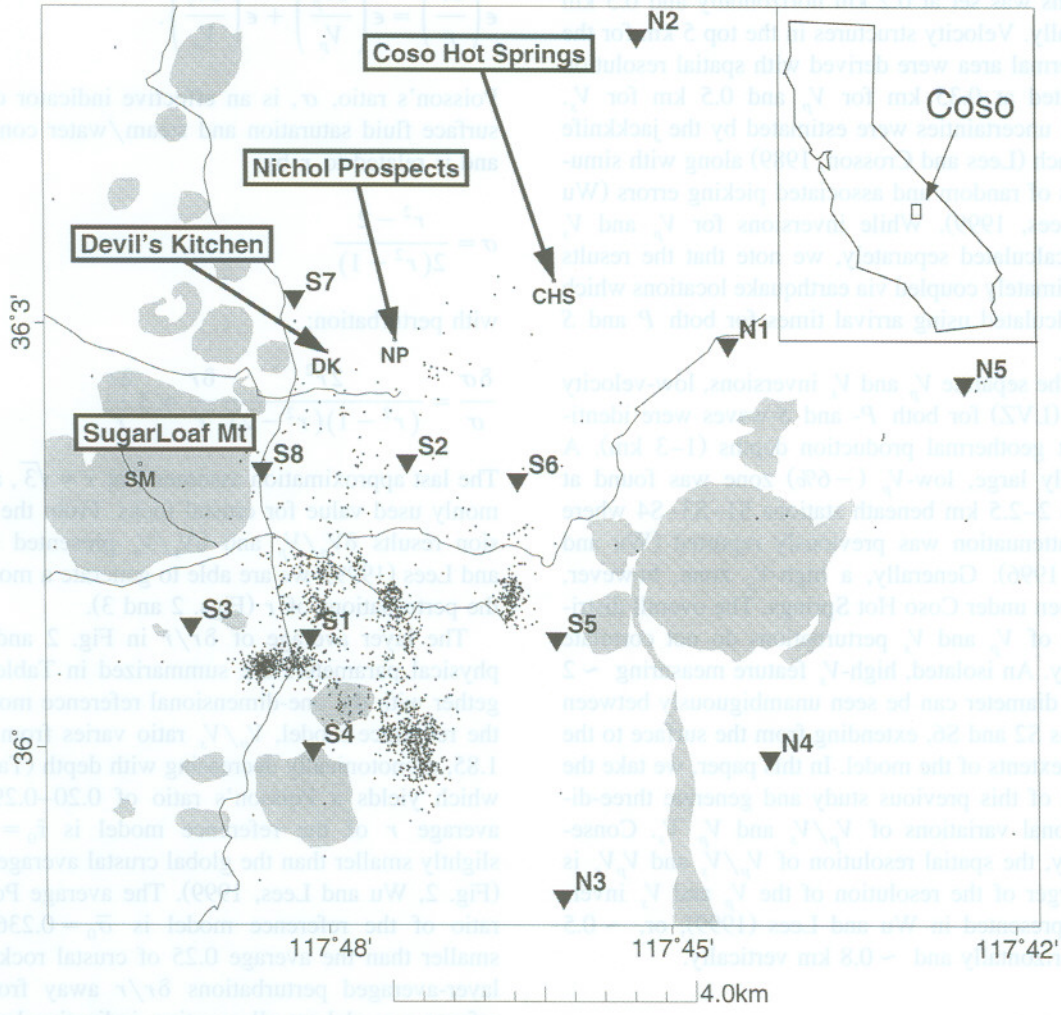

Fig. 1. Mapview of the geothermal field region at Coso, California. Inset is a California map showing the location of the target. Circular gray-shaded features in the west are rhyolite domes, the eastern gray-shaded features are other volcanics (Duffield and Bacon, 1981). Small dots represent seismic events used in this study, triangle symbols are seismic stations in Table 1 of Wu and Lees (1999) and important geographic locations are annotated: DK, Devil's Kitchen; NP, Nicol Prospects; CHS, Coso Hot Springs; SM, Sugarloaf Mountain.

direction in comparison to other clusters (Feng and Lees, 1998). Attenuation studies revealed a low-Q body deep in the southwestern part of the field shoaling to the north-northwest near Coso Hot Springs (CHS).

High-precision P- and S-wave traveltimes of 2104 microearthquakes with hypocenters <6 km were used to derive high-resolution three-dimensional compressional and shear velocity models (Wu and Lees, 1999). The methodology used followed that of Lees, (1992), including non-linear inversion with three-dimensional raytracing. Block size for the inversions was set at 0.2 km horizontally and 0.5 km vertically. Velocity structures in the top 5 km for the geothermal area were derived with spatial resolution estimated at 0.35 km for V_p and 0.5 km for V_s. Model uncertainties were estimated by the jackknife approach (Lees and Crosson, 1989) along with simulations of random and associated picking errors (Wu and Lees, 1999). While inversions for V_p and V_s were calculated separately, we note that the results are ultimately coupled via earthquake locations which are calculated using arrival times for both P and S waves.

In the separate V_p and V_s inversions, low-velocity zones (LVZ) for both P- and S-waves were identified at geothermal production depths (1–3 km). A spatially large, low-V_p (-6%) zone was found at depths 2–2.5 km beneath stations S1–S3–S4 where high attenuation was previously reported (Wu and Lees, 1996). Generally, a high-V_p zone, however, was seen under Coso Hot Springs. The overall distribution of V_p and V_s perturbations do not correlate directly. An isolated, high-V_s feature measuring ~ 2 km in diameter can be seen unambiguously between stations S2 and S6, extending from the surface to the lower extents of the model. In this paper, we take the results of this previous study and generate three-dimensional variations of V_p/V_s and V_p V_s. Consequently, the spatial resolution of V_p/V_s and V_pV_s is the larger of the resolution of the V_p and V_s inversions presented in Wu and Lees (1999), or, ~ 0.5 km horizontally and ~ 0.8 km vertically.

3. V_p/V_s distribution

There is a simple relationship between perturbations of V_p and V_s and those of V_p/V_s, the ratio of compressional and shear wave velocities. Let $r = V_p/V_s$, assuming small perturbations, and taking derivatives:

$$\frac{\delta r}{r} = \frac{\delta V_p}{V_p} - \frac{\delta V_s}{V_s}, \tag{1}$$

showing that the percentage perturbation of r is the difference of the perturbation of V_p and V_s. Consequently, errors in $\delta r/r$ are the sum of the errors in $\delta V_p/V_p$ and $\delta V_s/V_s$:

$$\epsilon\left(\frac{\delta r}{r}\right) = \epsilon\left(\frac{\delta V_p}{V_p}\right) + \epsilon\left(\frac{\delta V_s}{V_s}\right). \tag{2}$$

Poisson's ratio, σ, is an effective indicator of subsurface fluid saturation and steam/water conditions and is related to r by:

$$\sigma = \frac{r^2 - 2}{2(r^2 - 1)} \tag{3}$$

with perturbation:

$$\frac{\delta\sigma}{\sigma} = \frac{2r^2}{(r^2-1)(r^2-2)}\frac{\delta r}{r} \approx 3\frac{\delta r}{r} \tag{4}$$

The last approximation assumes that $r \approx \sqrt{3}$, a commonly used value for crustal rocks. From the inversion results $\delta V_p/V_p$ and $\delta V_s/V_s$ presented in Wu and Lees (1999), we are able to generate a model for the perturbations of r (Figs. 2 and 3).

The layer average of $\delta r/r$ in Fig. 2 and other physical parameters are summarized in Table 1 together with the one-dimensional reference model. In the reference model, V_p/V_s ratio varies from 1.63–1.85, monotonically decreasing with depth (Table 1), which yields a Poisson's ratio of 0.20–0.29. The average r of the reference model is $\bar{r}_0 = 1.705$, slightly smaller than the global crustal average 1.732 (Fig. 2, Wu and Lees, 1999). The average Poison's ratio of the reference model is $\bar{\sigma}_0 = 0.236$, also smaller than the average 0.25 of crustal rocks. The layer-averaged perturbations $\delta r/r$ away from the reference model are all negative, indicating lower V_p relative to V_s throughout the whole region. The layer-averaged perturbation for depth 2.0–3.5 km (3 layers) is as large as -5%, which is the largest in

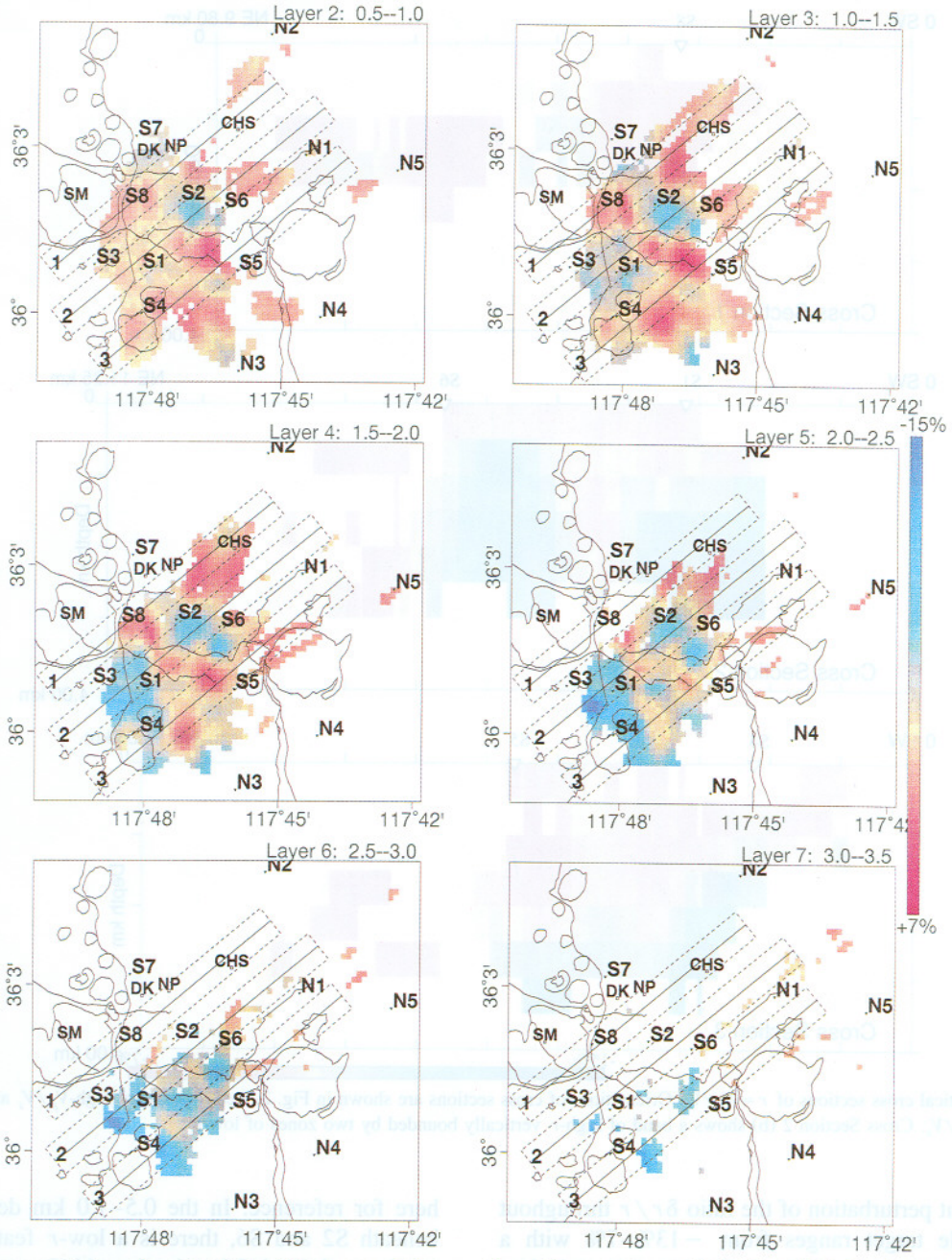

Fig. 2. Percent perturbation of $r = V_p/V_s$ for different crustal layers at Coso. The average perturbation is -1.8%. The largest perturbation is -13%. Red regions are high-r and blue areas are low-r.

the depth profile in Table 1. These three layers, however, are not well sampled in the inversion except for depth range 2.0–2.5 km which is in the deeper range of the geothermal production zone. The average r is estimated to be about 1.62 ($\sigma \approx 0.20$) in the depth range of geothermal production (1–3 km).

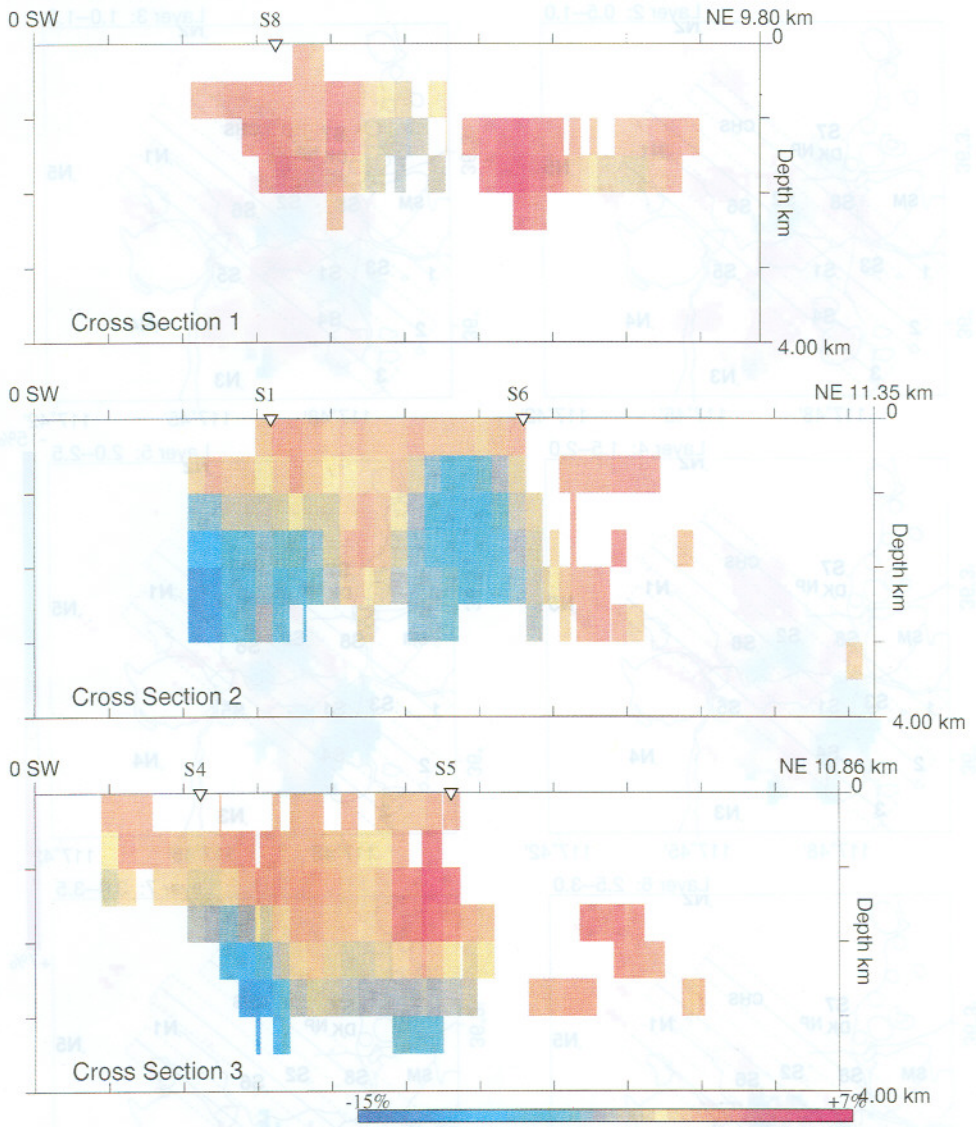

Fig. 3. Vertical cross sections of $r = V_p/V_s$. Orientations of cross sections are shown in Fig. 2. Red regions are high-V_p/V_s and blue areas are low-V_p/V_s. Cross Section 2 (b) shows a band of high-r vertically bounded by two zones of low-r.

Percent perturbation of the ratio $\delta r/r$ throughout the whole target ranges from -13%–7% with a negative average -1.8%, indicating that r is less than the reference model. The range of r is 1.49–1.98. Applying Eq. (4) yields an equivalent Poisson's ratio ranging from $\sigma = 0.15$–0.35. The average over the whole target is $\bar{\sigma} = 0.224$.

The main features of the three-dimensional distribution of r are presented in Fig. 2 and described here for reference. In the 0.5–1.0 km depth range, beneath S2 and S6, there is a low-r feature which continues through 3 km depth and bifurcates at depth between 2.0–2.5 km. Northwest of S5, there is an extremely high-r region ($+5.5\%$ perturbation) which also continues to the bottom of the model, reaching its peak value at depth 1.0–1.5 km. At depths > 1.0 km, a broad low-r region is found around S1–S3–S4 and continues to at least 3 km depth. This feature

Table 1
Depth profile of perturbations

Layer	Depth (km)	V_{p0}	V_{s0}	r_0	V_p	V_s	$\delta V_p/V_p$	$\delta V_s/V_s$	$\delta r/r$	$\delta\Psi/\Psi$
1	0.0–0.5	4.50	2.43	1.85	4.50	2.43	+0.02	+0.09	−0.07	+0.12
2	0.5–1.0	4.51	2.59	1.74	4.48	2.59	−0.58	+0.16	−0.78	−0.39
3	1.0–1.5	4.92	2.97	1.66	4.86	2.96	−1.27	−0.26	−1.10	−1.55
4	1.5–2.0	4.92	2.97	1.66	4.80	2.95	−2.39	−0.55	−1.83	−2.89
5	2.0–2.5	5.46	3.15	1.73	5.25	3.14	−3.81	−0.40	−3.54	−4.26
6	2.5–3.0	5.46	3.15	1.73	5.21	3.16	−4.62	+0.21	−5.11	−4.59
7	3.0–3.5	5.54	3.27	1.69	5.42	3.32	−2.34	+1.54	−4.74	−1.22
8	3.5–4.0	5.54	3.27	1.69	5.51	3.27	−0.50	−0.05	−0.44	−0.60
9	4.0–5.5	5.58	3.42	1.63	5.58	3.42	−0.01	+0.03	−0.04	+0.02

The three columns are reference values from one-dimensional reference model shown in Fig. 2 of Wu and Lees (1999). The next two columns are inversion results of Wu and Lees (1999) and the last two columns are perturbations of r and Ψ. All values are layer average. The perturbation values shown in the last four columns are percentage figures, e.g., $100 * \delta r/r$ for V_p/V_s ratio.

corresponds to a low-Q anomaly interpreted as a possibly fossil magmatic channel in attenuation studies (Wu and Lees, 1996). High-r structures east of station S8 and south of Coso Hot Springs are also prominent. Overall, high- or normal-r regions are extensive and well connected while low-r regions are relatively isolated, especially at shallow depths. However, low-r regions usually exhibit larger perturbation magnitudes than high-r regions. A high-r swath runs approximately northwest to southeast and separates low-r regions around S2–S6 and S1–S3–S4 This anomaly corresponds to a circular low-V_s region identified earlier (Wu and Lees, 1999). A prominent, high-r feature, ~1 km wide, is seen in cross section 2 located between two low-r structures underlying stations S1 and S6 (Fig. 3). This high-r zone extends from the surface to depth and is part of the previously noted circular feature.

For igneous rocks, such as basalt and granite, r generally decreases as temperature increases, and r increases as pressure increases (Fig. 4) (Christensen, 1989). With average $r \approx 1.62 < 1.732$, Coso rocks are probably hotter than average crustal rocks under similar pressure state or depth. Based on these results, the southwestern part of the target region is probably hotter than the northeastern part. If we use r as relating inversely to temperature, Fig. 2 bares some similarity to measured isotherms of Combs (1980) with contours generally centered off the southeastern edge of Sugarloaf mountain (see Fig. 14d in Wu and Lees, 1996). On the other hand, fluid saturated rocks also have elevated r, so a low-r may indicate either fluid depletion or elevated temperature. Regions S2–S6 and S1–S3–S4 exhibit depressed r.

V_p/V_s ratio found in this study is consistent with the field measured result of 1.57 at Devil's Kitchen (DK) (Combs and Rostein, 1976). Unfortunately, Devil's Kitchen lies beyond the boundary of the currently resolved region and a direct comparison is not possible. However, regions close to Devil's Kitchen show a slightly low-$r \approx 1.62$ at depth 1.0–1.5 km. Considering the excessive heat observed there, we speculate that there exists a large, low-r region immediately below Devil's Kitchen.

Model errors determined by the jackknife method (Fig. 5) are as large as $\pm 2.3\%$ around the edge of the model and north of S2. In the central S2–S3–S4–S5 region, errors are about $\pm 1\%$ at all depths. Errors of this magnitude are unlikely to change the general picture of r variation which is observed to be as large as 15%. In the current investigation, only those features with r variations exceeding 5% are interpreted.

4. Relation of V_p/V_s and Coso lithology

As a rule of thumb, V_p and r are lowest for quartz-rich silicates and larger for crustal rocks of more mafic composition (Koch, 1992). Poisson's ratio, σ, and thus r, have been used as lithologic indicators based on laboratory experiments of porous, sedimentary rocks (Toksöz et al., 1976; Tatham,

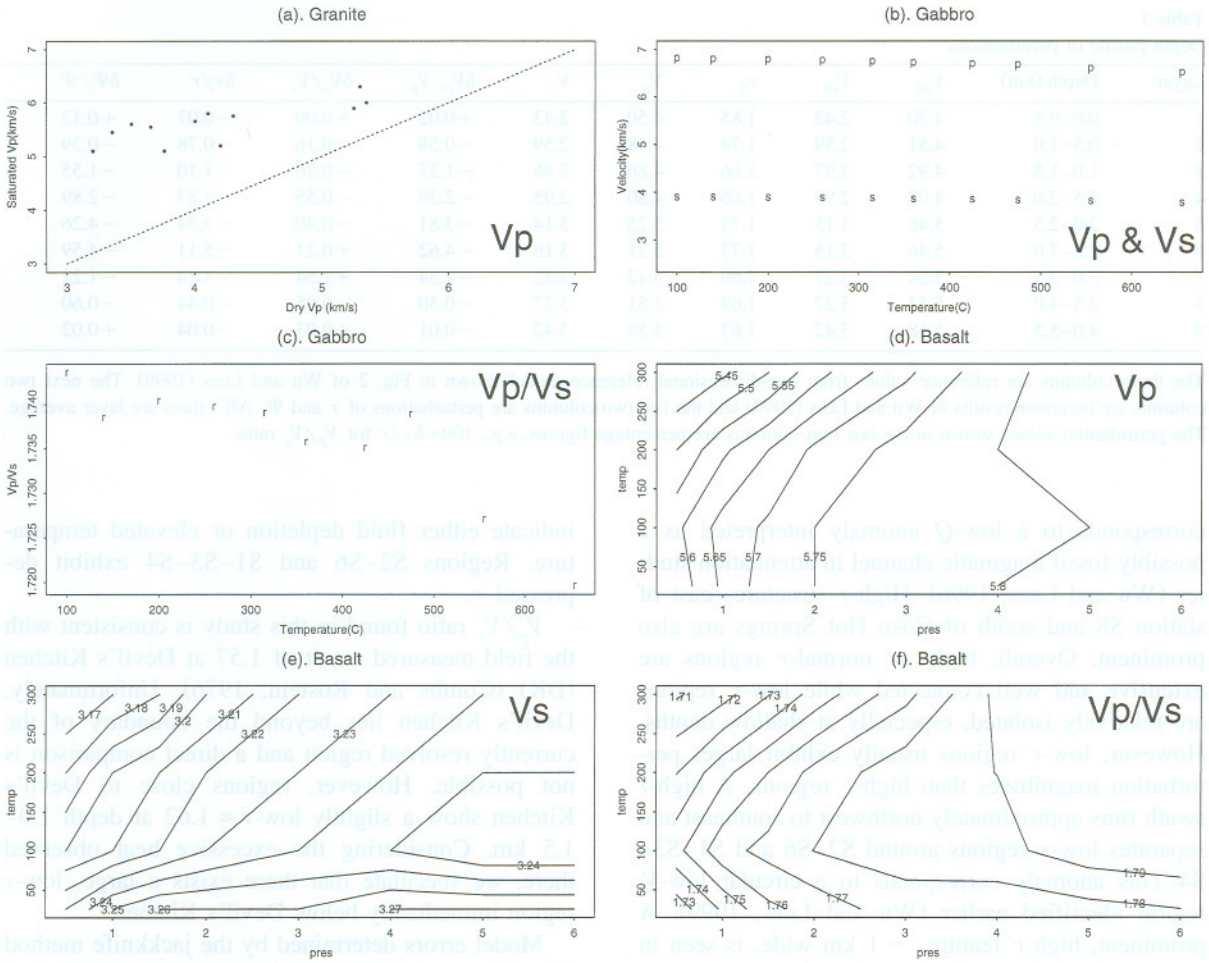

Fig. 4. Laboratory measurements of rock properties for some common igneous rocks under variable physical conditions (after Christensen, 1989). The first three plots are for granite and gabbro and the last three figures are for basalt. (a) Effects of fluid saturation on *P*-wave velocity at room temperature. Each dot represents a granitic sample with varying degrees of saturation and porosity. Dashed line represents equal velocities in dry and saturated states. At room temperature, saturated granite has higher compressional velocity. (b) Effects of temperature on *P*- and *S*-wave velocity of Gabbro. Marker "p" indicates a measurement of *P*-wave velocity and "s" indicates a measurement of *S*-wave velocity. Hot rocks have lower velocities. (c) Velocity ratio $r = V_p/V_s$ from (b) are plotted. Like V_p and V_s, ratio r generally decreases with temperature. (d) Effects of temperature and ambient pressure on V_p of basalt. The iso-velocity lines generally trend to the upper right, indicating that temperature and pressure tend to have opposite effects on velocity. (e) Effects of temperature and ambient pressure on V_s of basalt. The iso-velocity lines trend upright as in V_p case. The slopes are different although they have similar trends. Temperature appears to have a relatively larger effect on V_s than ambient pressure. In another words, V_s is a more sensitive indicator of temperature changes. (f) Effects of temperature and ambient pressure on the V_p/V_s ratio of basalt. There appear to exist two trends of iso-r lines depending on whether temperature is $> 100°$ or when temperature is $< 100°$.

1982). Since we do not have a detailed structural map of subsurface geology at Coso, it is premature to determine lithology from r variations and surface geology. In a heavily faulted and extensively intruded area like Coso, it is presumptuous to extrapolate observed surface lithology down several hundred meters. In the present study we restrict our interpretation to the broad relationship between surface lithology and shallow r distributions.

In general, shallow variations of r do not correspond to the surface geology as mapped by Duffield and Bacon (1981). There are, however, some excep-

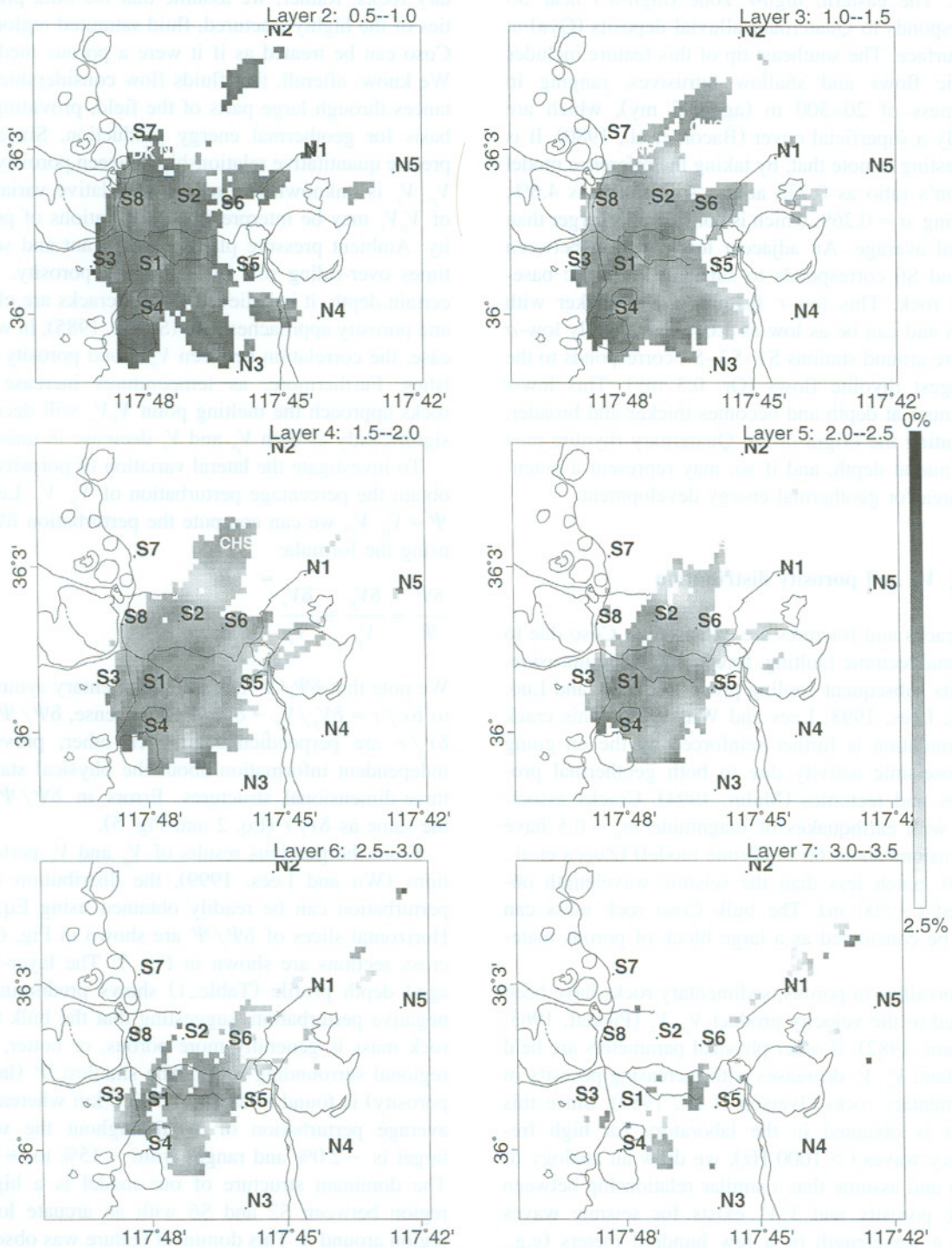

Fig. 5. Jackknife error estimates of $\delta r/r$ perturbations are also appropriate for $\delta\Psi/\Psi$ perturbations. In most regions errors are $\sim 1.0\%$. The largest errors (up to 2.3%) are seen between Coso Hot Springs (CHS) and station S2, and around the edge of the model.

tions. The eastern, high-r zone (high-σ) near S5 corresponds to Quaternary alluvial deposits (Qya) at the surface. The southeast tip of this feature includes dacitic flows and shallow intrusives, ranging in thickness of 20–300 m (age 3.5 my), which are clearly a superficial cover (Bacon et al., 1980). It is interesting to note that, by taking the reference model Poison's ratio as 0.236 at this spot, $\delta r/r$ is 4.6%, yielding $\sigma = 0.269$, which is considerably larger than crustal average. An adjacent low-r region between S2 and S6 corresponds to surficial Mesozoic basement rock. This low-r feature grows thicker with depth and can be as low as 1.63. The slightly low-σ feature around stations S1–S3–S4 corresponds to the youngest rhyolite flows (Qr, 0.3 my). This low-r continues at depth and becomes thicker and broader, indicating the origin of the Quaternary rhyolite may continue at depth, and if so, may represent a potential area for geothermal energy development.

5. V_p V_S and porosity distribution

Cracks and fractures are extensive at Coso due to regional tectonic faulting, forced magmatic intrusion, and its subsequent cooling process (Shalev and Luo, 1995; Lees, 1998; Lees and Wu, 1999). This crack accumulation is further reinforced by the on going microseismic activity due to both geothermal processes and tectonics (Malin, 1994). Cracks associated with earthquakes of magnitude $m_b = 0.5$ have dimensions about 60 m (Brune model) (Zucca et al., 1994), much less than the seismic wavelength observed (~ 500 m). The bulk Coso rock mass can thus be considered as a large block of porous material.

Porosities in porous, sedimentary rocks have been related to the velocity product V_p V_s (Pickett, 1963; Tatham, 1982). If other physical parameters are held constant, V_p V_s decreases with increasing porosity in sedimentary rocks (Iverson et al., 1989). Since this result is obtained in the laboratory for high frequency waves (> 1000 Hz), we draw an analogy of scale and assume that a similar relationship between crack porosity and V_pV_s exists for seismic waves with a wavelength of a few hundred meters (e.g., wavelength ~ 500 m at 10 Hz). We are not suggesting that rocks in the Coso field behave like sedimentary rocks. Rather, we assume that the bulk properties of the highly fractured, fluid saturated regions of Coso can be treated as if it were a porous medium. We know, afterall, that fluids flow considerable distances through large parts of the field, providing the basis for geothermal energy production. Since the precise quantitative relationship between porosity and V_p V_s is unknown at Coso, only relative variations of V_pV_s may be interpreted as fluctuations of porosity. Ambient pressure plays a significant and sometimes over-riding role in controlling porosity. At a certain depth, it is believed that all cracks are closed and porosity approaches zero (Suppe, 1985), in which case, the correlation between V_pV_s and porosity vanishes. Furthermore, as temperatures increase and rocks approach the melting point V_pV_s will decrease significantly as both V_p and V_s decrease in unison.

To investigate the lateral variation of porosity, we obtain the percentage perturbation of V_p V_s. Letting $\Psi = V_p$ V_s, we can compute the perturbation $\delta\Psi/\Psi$ using the formula:

$$\frac{\delta\Psi}{\Psi} = \frac{\delta V_p}{V_p} + \frac{\delta V_s}{V_s}. \tag{5}$$

We note that $\delta\Psi/\Psi$ has a complimentary symmetry to $\delta r/r = \delta V_p/V_p - \delta V_s/V_s$. In a sense, $\delta\Psi/\Psi$ and $\delta r/r$ are perpendicular to each other, providing independent information about the physical state of three-dimensional structures. Errors in $\delta\Psi/\Psi$ are the same as $\delta r/r$ (Eq. 2 and Fig. 5).

From the previous results of V_p and V_s perturbations (Wu and Lees, 1999), the distribution of Ψ perturbation can be readily obtained using Eq. (5). Horizontal slices of $\delta\Psi/\Psi$ are shown in Fig. 6 and cross sections are shown in Fig. 7. The layer-averaged depth profile (Table 1) shows predominantly negative perturbation, suggesting that the bulk Coso rock mass is generally more porous, or hotter, than regional surrounding rocks. The smallest Ψ (largest porosity) is found at depths 1.5–3.0 km whereas the average perturbation of Ψ throughout the whole target is -2.0% and ranges from -15% to $+12\%$. The dominant structure of our model is a high-Ψ region between S2 and S6 with an arcuate low-Ψ region around it. This dominant feature was observed earlier in V_s and r studies. We discuss this feature in detail in the next section in relation to fluid flow.

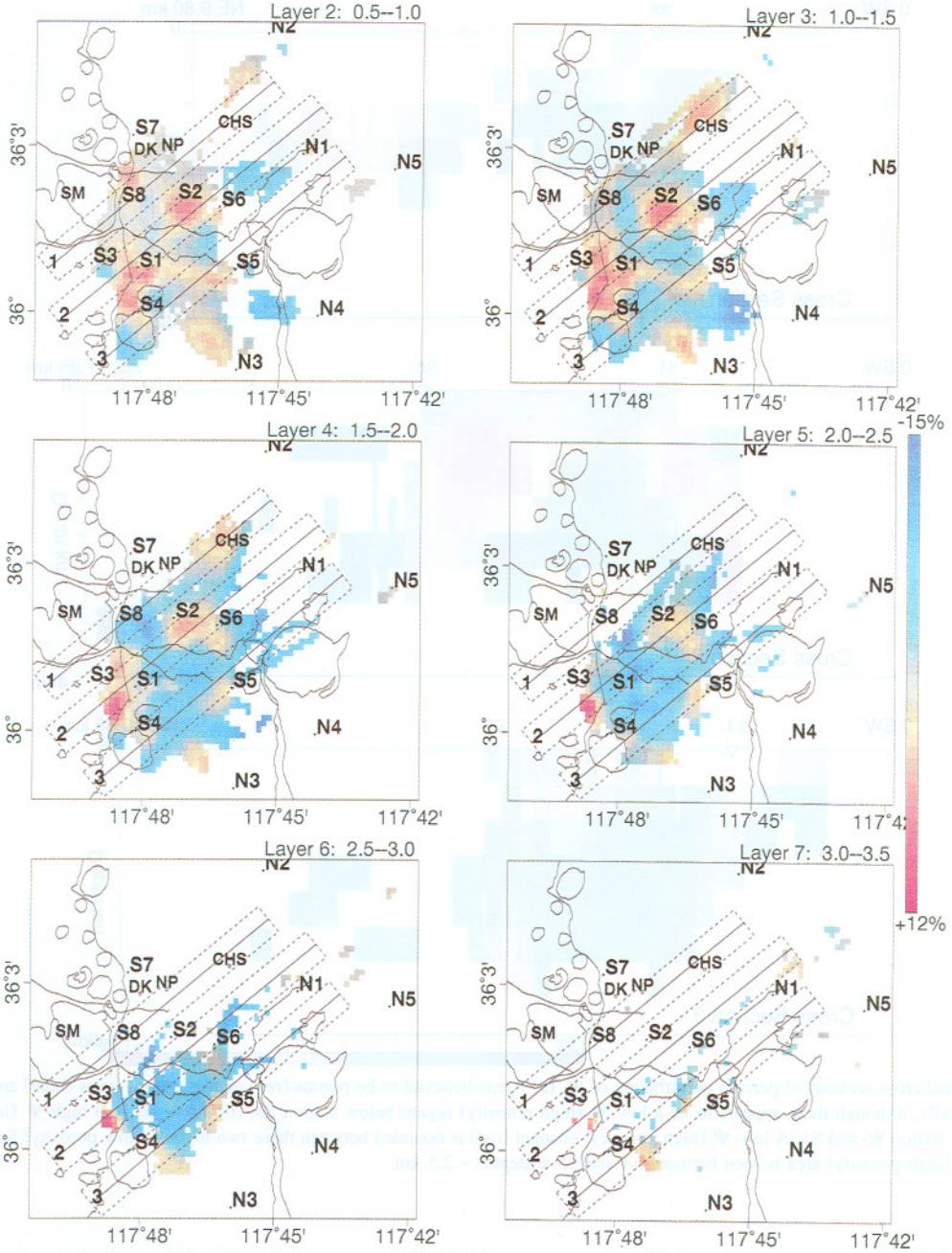

Fig. 6. Percent perturbations of $\Psi = V_p V_s$. Red areas are high-Ψ; blue areas are low-Ψ. In sedimentary rocks high-Ψ indicates low porposity and low-Ψ is high porosity. The average perturbation in Ψ is -2.0%.

A high-Ψ channel is found below S1–S3–S4 (Figs. 6 and 7b) and corresponds to the high attenuation channel in Wu and Lees (1996) and low-r feature discussed above (Fig. 3). It is consistent with the suggestion that this is the location of a rising/fossil magmatic body and is probably the hot,

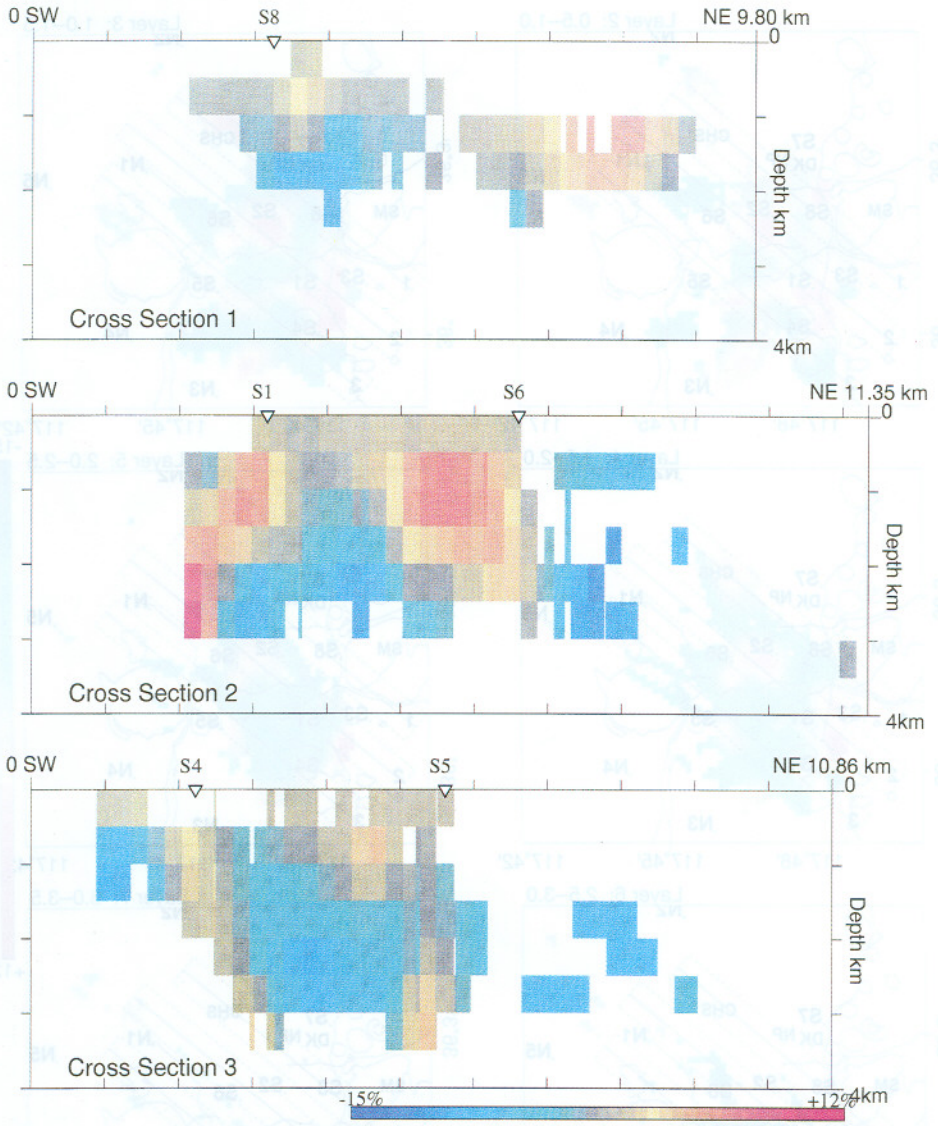

Fig. 7. Vertical cross sections of percent perturbation of Ψ. (a) Areas believed to be porous (red) or less porous areas (blue) are not clearly defined laterally, although there appears to be a low-Ψ (high porosity) region below station S8. (b) There are two high-Ψ (low porosity) zones below station S6 and S1. A low-Ψ (high porosity) channel (red) is bounded between these two high-Ψ (low porosity) features. (c) A red, low-Ψ (high porosity) area is seen between S4 and S5 at depth $\sim$2.5 km.

low porosity and unfractured core of an intrusion. The dark shaded region at the center of cross section 2 has low-Ψ and may be actually a conduit/reservoir for fluid flow, and hence saturated as shown by high-r in Fig. 3. The unfractured (low porosity) neighbor of this block contains less fluid and thus has lower r. This low-Ψ feature is $\sim$1.5 km in width and broadens with depth.

The edge of Sugarloaf Mountain generally exhibits medium Ψ. A very low-Ψ region is found east of S4 and probably dips east with depth. At depths 2.0–2.5 km, this feature is seen at $\sim$1 km

south of station S5 and ~ 2.0 km east of station S4. It is interesting to note that this structure corresponds to a schematically presumed east-dipping fault (Leslie, 1991) (Fig. 8). The high-Ψ feature may be a trace of this faulting, if it actually exists. This feature is separated from the northern S1–S5 low-Ψ (highly porous) zone by an east–west trending high-Ψ (low porosity and presumably less permeable) barrier (width ~ 0.5 km) which is most prominent down to depth ~ 1.5 km. This barrier runs nearly east–west from S1 to S5 at depth < 1.5 km. At S1, this high-Ψ barrier joins a broad, north–south trending high-Ψ zone at the edge of Sugarloaf Mountain and forms a ''T''-shaped high-Ψ (low porosity) barrier centered at S1–S3–S4 region.

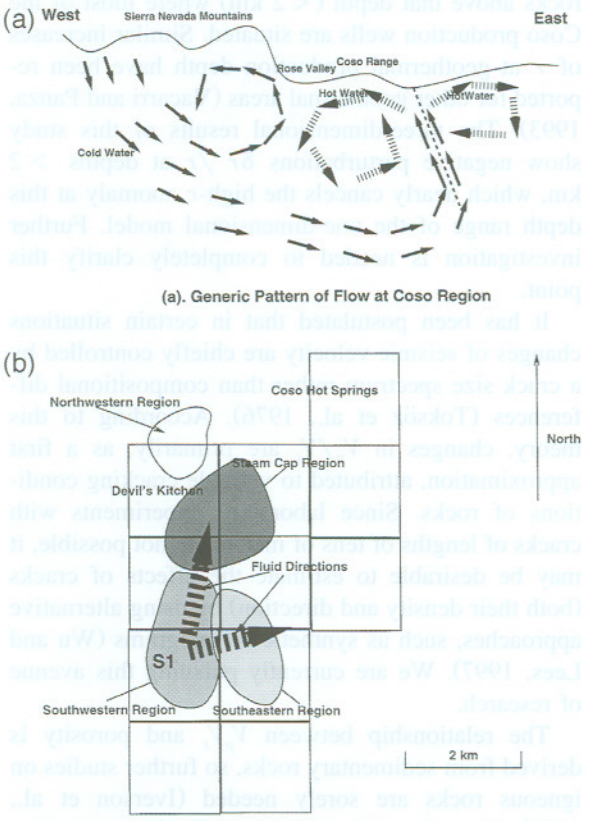

Fig. 8. Geothermal fluid flows models. (a) Ground water cycle at Coso (modified from Leslie, 1991: Fig. II-2A). Water from Sierra Nevada and Coso Range recharges the geothermal system. Hot waters reach the surface through an east-dipping system of faults and fractures. (b) Map of the geochemically defined sub-regions at Coso geothermal area (modified from Leslie, 1991: Fig. II-3). The hypothetical fluid-mixing direction is denoted by bold arrows. Rectangles refer to numbered BLM (Bureau of Land Management) tracts.

The vertical extent of the above mentioned features is seen more clearly on vertical cross sections through the model (Fig. 7). On profile 1 (Fig. 7a), the demarcation between low and high-Ψ zones is not particularly prominent. Profile 2, however, shows that the vertical extent of the S1–S5 low-Ψ zone extends below the bottom of the model and suggests that hot waters rise from depth, approximately half way between stations S1 and S6. Profile 3 shows more low-Ψ zones than Profiles 1 and 2, but does not exhibit large variations in Ψ.

6. Porosity and geothermal fluid flow

In relating porosity to fluid flows in the region, we note that while low porosity suggests less permeability, high porosity does not necessarily indicate high permeability. High permeability depends on the connectivity of pores and cracks. The most salient features of $\delta\Psi/\Psi$ distribution (Fig. 6) is a high-Ψ region between S2–S6 which reaches its peak at about 1–1.5 km depth. This high-Ψ feature extends from the surface to at least 3 km depth and is probably a barrier to geothermal fluid flow. South and west of S2–S6, there is a circular band of low-Ψ region, exhibiting high-r (Fig. 2) which is probably fluid-saturated. The extent of this high porosity band is parallel to a suggested fluid-mixing directions discussed by Leslie (1991) (Fig. 8b). If we follow Leslie's model, fluid flows are northbound west of S2 and eastbound south of S2. The source of the fluid flow, probably originating close to S1 and flowing northeast, is separated by the less permeable rock body in the area between S2 and S6. The source flow is forced to branch and flow eastward and northward.

A previous chemical study of production fluids defined a plume of thermal fluid that rises from depth in the south and spreads out towards the north and east (Moore et al., 1989). The measured Cl and CO_2 concentration fans out from the center southeast of Sugarloaf and decreases to the north and east (Moore et al., 1989). However, it has also been observed that fluids flow from north to south (F.

Monastero, pers. commun., 1996). This is not unreasonable, considering the presence of faults and fractures with all orientations (Roquemore, 1980). Fluid flow is generally subject to fracture geometry. If fluids rise from depth along faults dipping northward, the apparent flow will be southbound and vice versa. Further geochemical studies divide the geothermal fluids into four distinctive sub-regions which fall in the high porosity areas of the two arms of the above circular feature (Fig. 8b) (Leslie, 1991). The four subregions have different chemical signatures typical of different stages of fluid mixing. A hypothetical fluid mixing model has been put forward based on these observations (Fig. 9) and is consistent with our porosity distribution (Fig. 6, Layers 3 and 4; Fig. 8).

7. Discussion

Seismic velocity variations depend on many physical conditions and it is often difficult to isolate one specific source for observed variations in three-dimensional inversions. Composition, fractures, cracks, porosity, saturation condition, temperature as well as ambient pressure all play a role in velocity variations (Sanders et al., 1995). Composition may, in some sense, be more fundamental than other factors because it is an intrinsic property of the local rock. Generally, igneous rocks exhibit higher velocity than sedimentary rocks at laboratory scales. Both P and S velocities decrease with increasing temperature (Fig. 4) (Christensen, 1989), although the rates of decrement of P- and S-waves are different. V_p decreases faster than V_s and the ratio $r = V_p/V_s$ decreases with increasing temperature (Fig. 4c). Randomly fractured media have both smaller V_p and V_s while V_p decreases slower than V_s, such that r increases. Ambient pressure also affects seismic velocity with V_p, V_s and r each increasing with pressure (Fig. 4) (Christensen, 1989). As can be seen, the above discussion highlights the complications involved in interpreting our data.

The presence of fluids further complicates interpretation. Fluid saturation generally induces higher P-wave velocity (Fig. 4a) and saturated, unconsolidated sediments typically have high-V_p/V_s ratios (Nicholson and Simpson, 1985). Saturation conditions can be inferred from the comparison of V_p and V_s data. V_p is expected to increase when saturation increases while V_s remains nearly the same, driving V_p/V_s higher (Ito et al., 1979). However, partial melt may decrease V_p and fluid saturated zones will have a net low-V_p, low-V_s and high-V_p/V_s (Walck, 1988). In our model, a few regions with low-V_p, low-V_s and high-V_p/V_s are identified: about 0.5–0.8 km northeast of station S1 at depth 1.5–2.5 km. Note there are several production wells close to this site (Moore et al., 1989).

We note that overall, r decreases with depth (Table 1). The increase of r at around 2–3 km depth in the 1-D model indicates the abnormal heating of rocks above that depth (< 2 km) where most of the Coso production wells are situated. Similar increases of r at geothermal production depth have been reported for other geothermal areas (Vacarri and Panza, 1993). The three-dimensional results of this study show negative perturbations $\delta r / r$ at depths > 2 km, which nearly cancels the high-r anomaly at this depth range of the one-dimensional model. Further investigation is needed to completely clarify this point.

It has been postulated that in certain situations changes of seismic velocity are chiefly controlled by a crack size spectrum rather than compositional differences (Toksöz et al., 1976). According to this theory, changes in V_p/V_s are primarily, as a first approximation, attributed to variable cracking conditions of rocks. Since laboratory experiments with cracks of lengths of tens of meters are not possible, it may be desirable to estimate the effects of cracks (both their density and direction) by using alternative approaches, such as synthetic seismograms (Wu and Lees, 1997). We are currently pursuing this avenue of research.

The relationship between V_pV_s and porosity is derived from sedimentary rocks, so further studies on igneous rocks are sorely needed (Iverson et al., 1989). Since the analogy made earlier between pores in sedimentary rocks and microcracks in igneous rocks on the scale of Coso is hard to prove in laboratories, in situ measurements may be used to calibrate the relationship between V_p V_s and bulk porosity. Another option is through numerical modeling of seismic wave propagation in cracked media (Wu and Lees, 1997). Three-dimensional porosity

anomalies provide strong constraints on fluid flow models, and, if combined with measured fluid flow in the field, will give us useful information about permeability. In an interesting application, a locally calibrated, empirical relation has been used to extract material properties, such as porosity, permeability and shear modulus, from velocity studies (Yamamoto et al., 1994). In the future, similar empirical conversions may be determined for the Coso region.

8. A magmatic intrusion model for Coso

The cumulative plot of rhyolitic rock volume versus age at Coso suggests that the past history of magmatic eruption will continue into the future with lapses of the order of thousands of years (fig. 5.21, Duffield et al., 1980). The associated magma plexus is probably still molten and may be close to the surface. All available geophysical evidence suggests the existence of an anomalous, probably magmatic body located > 5 km below the triangle formed by S1–S3–S4 (Walck and Clayton, 1987; Sanders et al., 1988; Caruso and Malin, 1993; Wu and Lees, 1996; Feng and Lees, 1998; Wu and Lees, 1999). Most of the related geothermal features are associated with this body. The general water cycle in this region is shown in Fig. 8a as modified from Leslie (1991). Water from the high Sierra Nevada and Coso Range flows at depth and is heated around the suspected hot igneous body and turns up around S1–S3–S4 through fractures caused by earlier intrusions and regional tectonics. The upwelling hot water spreads out horizontally along the local faulting pattern, forming the source waters for the geothermal field. The supply of drainage water from Sierra Nevada and Coso Range covers the region southwest of S4. The development of fluid flow patterns, however, depends on local tectonics and faulting patterns, as they control, to a large degree, the permeability, porosity and temperature of the active field. A geothermal boundary recently found southwest of S4 confines the geothermal fluids to the northeast of S4 (Lees, 1997). This explains the absence of geothermal activity southwest of station S4.

In summary, we suggest the following tentative model for the last major magmatic intrusion at Coso as a guide to further research (Fig. 9). The center of the magma movement is close to stations S1–S3–S4. Hot magma arose from depth and spread out in all directions. It flowed due north and due east following the two pre-existing sets of faults. Northeast of the spreading center, there is a strong, unfractured rock body which is the high velocity, less porous,

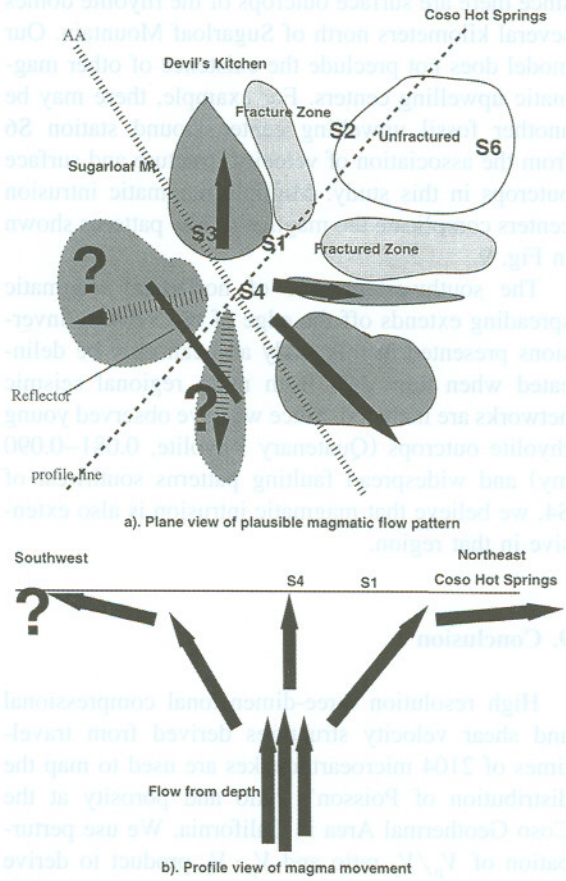

Fig. 9. Diagrammatic representation of the most recent period of magmatic activities at Coso geothermal area. Solid arrows represent correlations with inversion results and broken arrows are speculations. The solid line southwest of S4 is a geothermal boundary found by Lees (1997). Line AA separates regions controlled by the inversion results from those not controlled. Magma upwelled in the triangle S1–S3–S4 and migrated northwestward along pre-existing faults and erupted to the surface at Sugarloaf Mountain (Qr, 0.044 my). Coso Hot Spring and the S2–S6 region are not intruded. One flow went almost due south and created a rhyolite dome (Qr, 0.088 my). Two fracture zones were formed between magmatic flow and unintruded body in S2–S6. (a) Plane view of magma flows; (b) SW–NE cross section of the model. The trace of the profile is plotted as dashed line in (a).

fluid-depleted region seen in our tomographic inversions (stations S2–S6). Between the unfractured block of S2–S6 and magmatic intrusives are two highly fractured zones which today serve as conduits of geothermal fluid. These two zones form an arcuate feature around S2–S6. The actual magmatism appears more far-reaching than that shown in Fig. 9, since there are surface outcrops of the rhyolite domes several kilometers north of Sugarloaf Mountain. Our model does not preclude the existence of other magmatic upwelling centers. For example, there may be another fossil upwelling center around station S6 from the association of velocity structure and surface outcrops in this study. Multiple magmatic intrusion centers complicate the magmatic flow patterns shown in Fig. 9.

The southwestern side of horizontal magmatic spreading extends off the edge of our velocity inversions presented in this study and can only be delineated when new data from more regional seismic networks are included. Since we have observed young rhyolite outcrops (Quatenary Rhyolite, 0.081–0.090 my) and widespread faulting patterns southwest of S4, we believe that magmatic intrusion is also extensive in that region.

9. Conclusion

High resolution three-dimensional compressional and shear velocity structures derived from traveltimes of 2104 microearthquakes are used to map the distribution of Poisson's ratio and porosity at the Coso Geothermal Area in California. We use perturbation of V_p/V_s ratio and $V_p \cdot V_s$ product to derive Poisson's ratio and porosity and to delineate possible zones of intense heat, fracture accumulation and fluid saturation. Average Poisson's ratio at Coso is estimated to be 0.224 which is lower than the crustal average of 0.25. Two major features with low Poisson's ratio and low porosity are identified at geothermal production depth (1–3 km) near S2–S6 and S1–S3–S4. These two low-σ, less porous features are separated by a northwest–southeast trending, arcuate, high Poisson's ratio and high porosity band. The width of this circular structure is 0.8–1.2 km. This highly porous feature is linked to the previously reported structure in V_s tomography and is suspected to be fluid-saturated, probably representing a conduit or reservoir of geothermal fluid. The east–west and north–south arms of the arc correlate well with the observed mainstream fluid flow directions and are probably the main avenue through which hot water is transported from the heat center around S1–S3–S4. The vertical, low-σ and low porosity channel beneath triangle S1–S3–S4 corresponds to a high attenuation feature found in a previous Q inversion. We suggest that this is the hot, unfractured core of the last major magmatic event in the Coso field.

Acknowledgements

The authors thank the Navy Geothermal Program for funding this project (award #N68936-94-R-0139) and providing data. Helpful comments were provided by Craig Nicholson and Gary Pavlis. We acknowledge CalEnergy and Peter Malin (Duke University) for data and valuable advice.

References

Bacon, C.R., Duffield, W.A., Nakamura, K., 1980. Distribution of Quaternary rhyolite dome of the Coso Range, California: implications for the extent of the geothermal anomaly. J. Geophys. Res. 85, 2422–2433.

Caruso, C.W., Malin, P.E., 1993. Structure of the Coso geothermal field, Southern California, from seismic reflection and refraction data. EOS Trans. AGU 74 (43), 413.

Christensen, N.I., 1989. Seismic velocities. In: Carmichael, R.S. (Ed.), CRC Practical Handbook of Physical Properties of Rocks and Minerals. CRC Press, Boca Raton, FL.

Combs, J., 1980. Heat flow in the Coso geothermal area, Inyo County, California. J. Geophys. Res. 85, 2411–2424.

Combs, J., Rostein, Y., 1976. Microearthquake studies at the Coso Geothermal Area, China Lake, California. Proceedings of the 2nd United Nations Symposium on the Development and Use of Geothermal Resources 2, 909–916.

Duffield, W.A., Bacon, C.R., 1981. Geologic map of the Coso volcanic field and adjacent areas, Inyo County, California, U.S. Geological Survey, Miscellaneous Investigations Series, MAP-1200.

Duffield, W.A., Bacon, C.R., Dalrymple, G.B., 1980. Late Cenozoic volcanism, geochronology and structure of the Coso Range, Inyo County, California. J. Geophys. Res. 85, 2381–2404.

Feng, Q., Lees, J.M., 1998. Microseismicity, stress, and fracture within the Coso Geothermal Field, California. Tectonophysics 289, 221–238.

Hauksson, E., Haase, J.S., 1997. Three-dimensional V_p and V_p / V_s velocity models of the Los Angeles basin and central Transverse Ranges, California. J. Geophys. Res. 102, 5423–5453.

Holbrook, W.S., Gajewski, D., Krammer, A., Prodehl, C., 1988. An interpretation of wide-angle compressional and shear wave data in southwest Germany: Poisson's Ratio and petrological implications. J. Geophys. Res. 93, 12081–12106.

Ito, H., DeVilbiss, J., Nur, A., 1979. Compressional and shear waves in saturated rock during water-steam transition. J. Geophys. Res. 84, 4731–4735.

Iverson, W.P., Fahmy, B.A., Smithson, S.B., 1989. V_pV_s from mode converted P-SV reflections. Geophysics 54, 843–852.

Koch, M., 1992. Bootstrap inversion for vertical and lateral variations of the S wave structure and the V_p / V_s-ratio from shallow earthquakes in the Rhinegraben seismic zone, Germany. Tectonophysics 210, 91–115.

Lees, J.M., 1992. The magma system of Mount St. Helens: non-linear high resolution P-wave tomography. J. Volcanol. Geotherm. Res. 53 (1–4), 103–116.

Lees, J.M., 1997. Scattering from a vertical geothermal barrier at Coso, California. Seismol. Res. Letts. 68 (2), 318.

Lees, J.M., 1998. Multiplet analysis at Coso Geothermal Field. Bull. Seismol. Soc. Am. 88 (5), 1127–1143.

Lees, J.M., Crosson, R.S., 1989. Tomographic inversion for three dimensional velocity structure at Mount St. Helens using earthquake data. J. Geophys. Res. 94, 5716–5728.

Lees, J.M., Wu, H., 1999. P-wave anisotropy, stress, and crack distribution at Coso Geothermal Field, California. J. Geophys. Res. 104 (8), 17955–17973.

Leslie, B.W., 1991. Decay series disequilibria applied to the study of rock–water interaction in the Coso and the Salton sea geothermal systems, Ph.D. Thesis, Univ. of Southern Calif.

Malin, P., 1994. The seismology of extensional hydrothermal system. Geothermal Resources Council, Trans. 18, 17–22.

Moore, J.N., Adams, M.C., Bishop, B.P., Hirtz, P., 1989. A fluid flow model of the Coso geothermal system: Data from production fluids and fluid inclusions. In: Proceedings, Fourth Workshop on Geothermal Reservoir Engineering, Stanford University, 139–144.

Nicholson, C., Simpson, D.W., 1985. Changes in V_p / V_s with depth: implication for appropriate velocity models, improved earthquake locations, and material properties of the upper crust. Bull. Seismol. Soc. Am. 75, 1105–1124.

Pickett, G.R., 1963. Acoustic character logs and their applications in formation evaluation. J. Petrol. Tech. 15, 650–667.

Reasenberg, P., Ellsworth, W., Walter, A., 1980. Teleseismic evidence for a low-velocity body under the Coso Geothermal Area. J. Geophys. Res. 85, 2471–2483.

Roquemore, G., 1980. Structure, tectonics, and stress of the Coso Range, Inyo County, California. J. Geophys. Res. 85, 2434–2440.

Sanders, C.O., Ho, L.P., Rinn, D., Kanamori, H., 1988. Anomalous shear wave attenuation in the shallow crust beneath the Coso volcanic region, California. J. Geophys. Res. 93 (4), 3321–3338.

Sanders, C.O., Ponko, S.C., Nixon, L.D., Schwartz, E.A., 1995. Seismological evidence for magmatic and hydrothermal structure in Long Valley caldera from local earthquake attenuation and velocity tomography. J. Geophys. Res. 100, 8311–8326.

Shalev, E., Luo, M., 1995. Tomographic inversion for crack-density in Coso, California (abstract). EOS Trans. AGU 76 (46), F351, Spring Meet. Suppl.

Suppe, J., 1985. Principles of Structure Geology. Prentice-Hall, Englewood Cliffs, NJ.

Tatham, R.H., 1982. V_p / V_s and lithology. Geophysics 47, 333–344.

Toksöz, C., Cheng, H., Timur, A., 1976. Velocities of seismic waves in porous rocks. Geophysics 41, 621–645.

Vacarri, F., Panza, G.F., 1993. V_p / V_s estimation in southwestern Europe from P-wave and surface-wave tomography analysis. Phys. Earth Planet. Int. 78, 229–237.

Walck, M.C., 1988. Three-dimensional V_p / V_s variations for the Coso region, California. J. Geophys. Res. 93, 2047–2052.

Walck, M.C., Clayton, R.W., 1987. P-wave velocity variations in the Coso region, California, derived from local earthquake travel times. J. Geophys. Res. 92, 393–405.

Wu, H., Lees, J.M., 1996. Attenuation structure of Coso Geothermal Area, California, from P-wave pulse widths. Bull. Seismol. Soc. Am. 86, 1574–1590.

Wu, H., Lees, J.M., 1997. Boundary conditions on a finite grid: applications with pseudo-spectral wave propagation. Geophysics 62 (5), 1544–1550.

Wu, H., Lees, J.M., 1999. Three-dimensional P- and S-wave velocity structure of Coso geothermal area, California, from microseismic traveltime data. J. Geophys. Res. 104, 13217–13233.

Yamamoto, T., Nye, T., Kuru, M., 1994. Porosity, permeability, shear strength; crosswell tomography below an iron foundry. Geophysics 59, 1530–1541.

Zucca, J.J., Hutchings, L.J., Kasameyer, P.W., 1994. Seismic velocity and attenuation structure of the Geysers Geothermal Field, California. Geothermics 23, 111–126.